

# All Colloidal Supercapattery: Colloid@carbon Cloth Electrodes Meet “Water-in-Salt” Electrolyte

Xiangfei Sun,<sup>[a]</sup> Kunfeng Chen,<sup>\*[a]</sup> and Dongfeng Xue<sup>\*[b]</sup>

The pursuit of excellent electrochemical performance, non-flammability and environmental friendliness of aqueous batteries and supercapacitors has driven efforts to find high-energy yet reliable electrode materials and electrolyte solutions. Here, all colloidal supercapattery are developed using high-concentration “water-in-salt” electrolytes (LiTFSI-KOH) and pseudocapacitive colloid@carbon cloth as both positive and negative electrodes, which showed merits of batteries and supercapacitors. Ni/Co-colloid @carbon cloth positive and Fe-colloid @carbon cloth negative electrodes can be synthesized by *in situ*

electrochemical reaction. The maximum operating voltage of an aqueous colloidal supercapattery is 1.8 V, and the energy density can reach 73.98 Wh kg<sup>-1</sup> at a power density of 1799.5 W kg<sup>-1</sup>. The specific capacitance of the aqueous colloidal supercapattery still maintains 74.3% of the initial after 2000 cycles of charge/discharge measurement. The combination of quasi ion colloidal materials and “water-in-salt” electrolyte pave a profound way to achieve high energy and power ability simultaneously at the supercapattery device.

## Introduction

With the increasing aggravation of the global energy crisis, the development of clean and renewable new energy and corresponding energy storage devices are urgently needed.<sup>[1–4]</sup> Supercapacitors (SCs), also known as electrochemical capacitors, have excellent cycle life, high power density, fast charge and discharge speed and environmental benignity, regarded as one of the most promising energy storage devices.<sup>[5–7]</sup> However, compared with Li-ion batteries, the low energy density of capacitors severely limits their widespread applications.<sup>[8]</sup> Further enhancing the energy output density of the supercapacitor to achieve a supercapacitor device that is equivalent to moderate power and energy, has become a research hotspot in the international energy field. Supercapattories aim to harness the high power density and long cycle life of supercapacitors, while also incorporating the higher energy density characteristics of batteries. This is achieved by integrating two distinct types of energy storage mechanisms within a single device: an electrochemical double layer (EDL) capacitance for rapid charge/discharge cycles and a Faradaic pseudocapacitance or battery-like intercalation reaction for increased energy storage capacity. The key advantage of supercapattories lies in their ability to balance the power-to-energy ratio, offering both high power outputs suitable for burst applications and sufficient energy storage for longer durations. This unique blend of

properties positions Supercapattories as a promising candidate for addressing the challenges posed by the global energy crisis, especially in applications requiring frequent charge/discharge cycles and moderate to high energy demands, such as electric vehicles, portable electronics, and grid-scale energy storage systems.

According to equation  $E=1/2 CV^2$ , the energy density of the supercapacitor is proportional to the specific capacitance (C) of the electrode material and is proportional to the square of the potential window (V).<sup>[9–12]</sup> Therefore, the ratio capacitance and increasing the device operating potential window of the electrode material are two effective ways to improve the energy density of the supercapacitor. Notably, broadening the potential window necessitates strategies that ensure the stability and cyclic durability of the electrode materials. This involves meticulous material design, such as surface modifications to resist corrosion and degradation from the widened electrochemical environment, and the adoption of innovative electrolytes with high decomposition voltages and electrochemical stability. Additionally, exploring novel nanostructured electrode architectures and optimizing the electrode-electrolyte interface through interface engineering can further bolster the stability and performance of SCs under expanded potential windows. These concerted efforts not only promise to unlock the full potential of supercapacitors as viable alternatives to traditional energy storage devices but also pave the way for their widespread adoption in addressing the global energy challenge.

According to the different energy storage mechanisms, supercapacitor electrode materials are divided into electric double-layer electrode materials and pseudocapacitive electrode materials.<sup>[13–15]</sup> In the same active area, the pseudocapacitive electrode material can generate a larger specific capacity due to the electrochemical Faradaic reaction on the electrode surface and has greater development potential. RuO<sub>2</sub><sup>[16–18]</sup>, Fe<sub>3</sub>O<sub>4</sub><sup>[19–22]</sup>, V<sub>2</sub>O<sub>5</sub><sup>[23,24]</sup>, WO<sub>3</sub><sup>[25–27]</sup>, Co<sub>3</sub>O<sub>4</sub><sup>[28–30]</sup>, NiO<sup>[31,32]</sup> and

[a] X. Sun, K. Chen

Institute of Novel Semiconductors, State Key Laboratory of Crystal Materials, Shandong University, Jinan 250100, China  
E-mail: kufeng.chen@sdu.edu.cn

[b] D. Xue

Shenzhen Institute for Advanced Study, University of Electronic Science and Technology of China, Shenzhen 518110, China  
E-mail: dfxue@uestc.edu.cn

 Supporting information for this article is available on the WWW under <https://doi.org/10.1002/batt.202400380>

$\text{MnO}_2$ <sup>[33–35]</sup> have attracted extensive attention in electrode materials due to their various valence states in redox reactions. For example, Chen et al. found that the non-fixed  $\text{V}_2\text{O}_5$  nanosheet growing on the carbon cloth can provide a large amount of oxygen defect, accelerate the migration rate of ions on the surface of the electrode material, and show excellent electrochemical properties.<sup>[36]</sup> Shi et al. prepared amorphous  $\text{MnO}_2@\text{MWCNT}$  fiber through chemical vapor deposition that exhibited a high specific capacitance of  $8.5 \text{ F cm}^{-3}$  at  $1 \text{ cm}^{-3}$ .<sup>[37]</sup> Recent work has shown that transition bimetal oxide materials exhibit higher specific capacitance in supercapacitor applications. Due to factors such as synergistic effect, interfacial effect, and more reaction sites, bimetallic oxides can provide more abundant redox reactions, thus exhibiting excellent electrochemical performance and electrical conductivity. For anode materials,  $\text{FeOOH}$  is one of the ideal candidates due to its high capacitance value and environmental friendliness.<sup>[38,39]</sup> As mentioned above, reasonable design and combination of electrode materials greatly influence the electrochemical performance of electrode materials.

In addition, it is also a valid strategy for the design of a safe high ion conductive electrolyte to increase the energy output density of the supercapacitor. The electrolyte solution is a key component of the supercapacitor, and the function of transmitting electrons in the charge and discharge process is also dominated by the performance of the device. The existing electrolyte material has a solid electrolyte, an organic electrolyte and an aqueous electrolyte.<sup>[40]</sup> The organic electrolyte solution is applied to the supercapacitor due to its wider potential window in all types of electrolyte solutions. However, low ion conductivity, flammability, and safety show its poor potential in the future supercapacitor equipment market.<sup>[41,42]</sup> For a water-electrolyte storage device, the potential stability window of water-electrolyte due to water decomposition

reaction is  $1.23 \text{ V}$ .<sup>[43]</sup> In recent years, “water-in-salt” (WIS), as a new type of high voltage water system electrolyte, has attracted more and more attention from researchers in the field of electrochemical energy storage technology.<sup>[44]</sup> In WIS electrolytes, the salt mass is greater than that of water, reducing the water decomposition activity and allowing for an expanded potential stability window. Avireddy et al. immersed asymmetric  $\text{Ti}_3\text{C}_2//\alpha-\text{MnO}_2$  cell in  $21 \text{ M}$  potassium acetate water-in-salt electrolyte solution and the electrochemical stability window widened to  $2.2 \text{ V}$ . The results show that the electrolyte solution exhibits high ionic conductivity and the electrode material exhibits excellent electrochemical performance.<sup>[45]</sup>

To overcome the above shortcomings, through reasonable structural design, we prepared Ni/Co- and Fe-based colloidal materials as positive and negative electrode materials respectively by in-situ electrochemical oxidation method. Asymmetric supercapacitor based on the Ni/Co-based anode, Fe-based cathode and the LiTFSI-KOH electrolyte delivers a high energy density of  $73.98 \text{ Wh kg}^{-1}$  at a power density of  $1799.5 \text{ W kg}^{-1}$ . The capacity retention can be maintained at 74.3% after 2000 cycles. Furthermore, the Ni/Co-based colloidal electrode // Fe-based colloidal electrode asymmetric supercapattery device displays excellent flexibility and mechanical reliability, guaranteeing the supercapacitor can work properly under folding-unfolding states. Recently, a kind of supercapattery is designed to meet broad applications in the fields of industry, communications, medical equipment, military equipment and transportation.

## Results and Discussion

Figure 1 schematically illustrates the in-situ electrochemical oxidation processes. Firstly, the cleaned carbon fabric was then

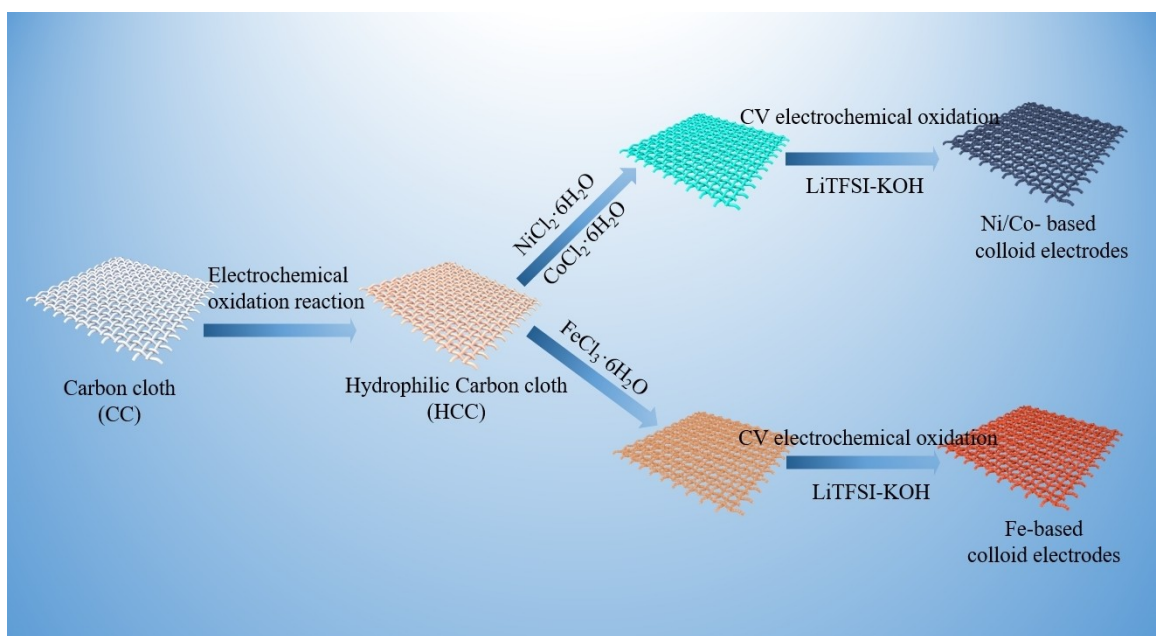
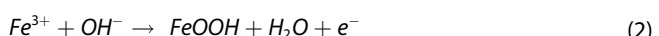
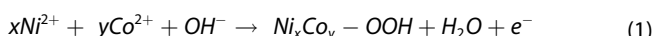


Figure 1. Schematic illustration of the in-situ preparation procedure of Ni/Co- and Fe-based colloid @carbon cloth electrodes.

immersed in  $(\text{NH}_4)_2\text{SO}_4$  solution and electrochemically oxidized to obtain an hydrophilic carbon cloth (HCC). Subsequently, Fe-based colloidal electrodes and Ni/Co-based colloidal electrodes were successfully synthesized by electrochemical oxidation of Fe and Ni/Co salts loaded on carbon cloth as current collectors by CV method, respectively. LiTFSI-4 M KOH was used as an electrolyte solution in CV electrochemical oxidation. The overall reaction pathway of Ni/Co-based colloidal electrode and Fe-based colloidal electrode can be illustrated as the following proposed chemical equations:



The morphological properties of the pristine carbon cloth (CC), HCC, and the activated electrodes were tested by digital images and scanning electron microscopy (SEM). Figure S1 shows photographs of the pristine CC, HCC, Ni/Co-based colloidal electrodes and Fe-based colloidal electrodes, respectively. After hydrophilic treatment, the color of the carbon cloth has changed significantly. The SEM images show no obvious difference between CC and HCC (Figure S2). However, it is immediately noticeable that Ni/Co-based colloidal electrodes and Fe-based colloidal electrodes have large and strong blocks attached to HCC compared to HCC.

The XRD patterns of CC, HCC, Ni/Co-based colloidal electrodes and Fe-based colloidal electrodes are shown in Figure 2a. Two diffraction peaks at  $25.8^\circ$  and  $43.4^\circ$  can be observed in the XRD patterns of all materials, which can be attributed to the (002) and (100) planes of amorphous carbon. We found no obvious change by comparing the X-ray diffraction (XRD) of CC and HCC. XRD patterns of Ni/Co-based colloidal electrodes and

Fe-based colloidal electrodes indicate that positive and negative electrodes are amorphous.

Furthermore, elemental mapping and EDS were performed to characterize the elemental distribution of Ni/Co-based colloidal electrodes (Figure 2b and S3) and Fe-based colloidal electrode materials (Figure 2c and S4). For Ni/Co-based colloidal electrodes, Ni, Co and O remained uniformly distributed on the substrate before and after the electrochemical reaction is completed. Thin film coating on the treated carbon cloth after the electrochemical reaction. In addition, Elements S and F derived from LiTFSI are found in both electrode materials. According to the EDS results, the ratio of Ni and Co is close to 1:2. The elemental mapping images of Fe-based colloidal electrode show that the chemical elements are composed of Fe, O, S and F.

Figure S5 shows the Raman spectra of CC and HCC. The typical peaks around  $1351$  and  $1582\text{ cm}^{-1}$  assigning to the D (the defect-induced mode) and G (the  $E_{2g}$  phonon modes of carbons) bands. The  $I_D/I_G$  of the carbon cloth after electrochemical oxidation was higher than that of the untreated carbon cloth, indicating that the defects on the HCC surface increased. Figure S6 shows an infrared absorption peak in the FTIR spectrum of HCC at  $3560\text{ cm}^{-1}$ , corresponding to the O-H stretching vibration, directly ensuring the increasing trend of hydroxyl ions in the system. The results of CC and HCC indicate that the appearance of the  $-OH$  functional group also indicated the successful preparation of HCC. The solvent recombination phenomenon of LiTFSI during electrochemical energy storage was investigated by Raman spectra characterization. The Raman spectroscopy of LiTFSI is illustrated in Figure 2d,f. When the LiTFSI addition amount is  $0.05\text{ mol/mL KOH}$  (water in salt), the peak that appears at  $281\text{ cm}^{-1}$  is attributed to the  $\text{CF}_3$  rocking vibration (Figure 2d).  $\text{CF}_3$  units have a negative potential that attracts cations, and almost all  $\text{CF}_3$  units interact with cations

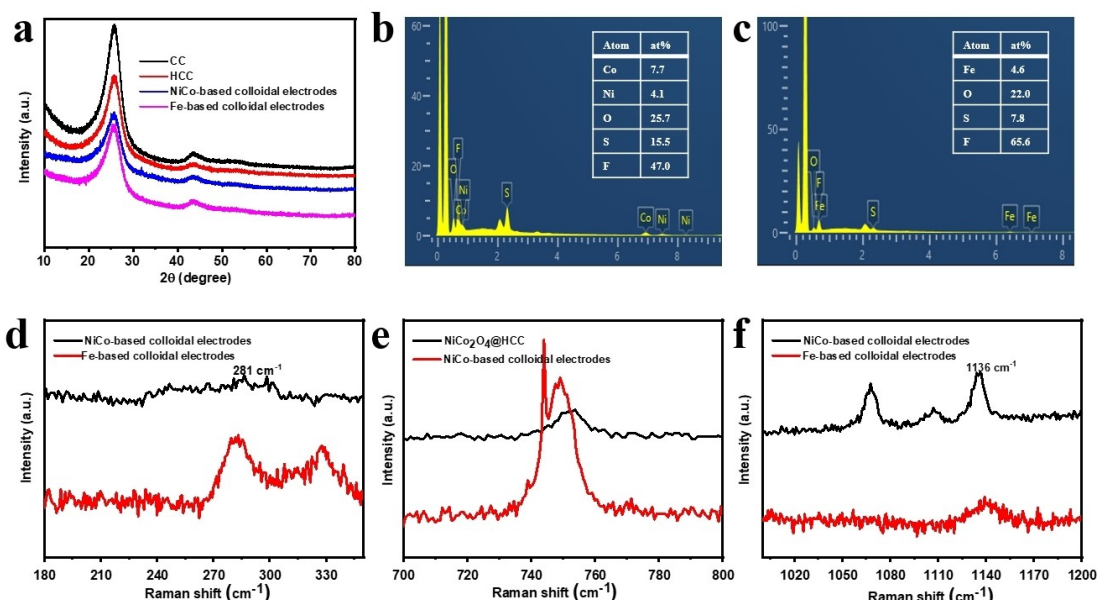


**Figure 2.** (a) XRD patterns of CC, HCC, Ni/Co-based colloidal electrodes and Fe-based colloidal electrodes. EDS of Ni/Co-based colloidal electrodes (b) and Fe-based colloidal electrodes (c). (d-f) Raman spectra of the Ni/Co-based colloidal electrodes and Fe-based colloidal electrodes.

when the LiTFSI concentration is low. Therefore, the features of  $\text{CF}_3$  rocking vibrations can hardly be detected. The strong band in the 743–746  $\text{cm}^{-1}$  spectral region is attributed to characteristic S–N–S bending vibrations (Figure 2e). Figure 2f shows the Raman spectra peak at 1136  $\text{cm}^{-1}$ , which is attributed to the  $\text{SO}_2$  symmetric stretching vibration.

X-ray photoelectron spectroscopy (XPS) was used to analyze the components and electronic characterization of Fe-based colloidal electrodes and Ni/Co-based colloidal electrodes. The survey spectrum results of Fe-based colloidal electrodes and Ni/Co-based colloidal electrodes show well-resolved peaks of Fe, O (Figure 3a) and Ni, Co, O species, respectively (Figure S7). The separation of  $\text{Fe } 2p_{3/2}$  and  $2p_{1/2}$  spin-orbit splits is large enough to allow partitioning of oxidation states and ablation of the more intense  $2p_{3/2}$  peak.<sup>[46]</sup> Figure 3b shows the XPS of  $\text{Fe } 2p$ , the peaks at 710.7 correspond to  $\text{Fe } 2p_{3/2}$  of  $\text{Fe}^{3+}$ , which indicates the presence of  $\text{FeOOH}$ . Figure 3d is the XPS of  $\text{Ni } 2p$ , the peaks at 874.2 eV and 856.5 eV are related to the  $\text{Ni } 2p_{1/2}$  and  $\text{Ni } 2p_{3/2}$ . The O 1s spectrum of Ni/Co-based colloidal electrodes indicated the peaks of the metal bonds at 532.2, and 533.4 eV.<sup>[47]</sup> Figure 3e shows the XPS spectra of  $\text{Co } 2p$  for Ni/Co-based colloidal electrodes. The test result indicates that the oxidation states of Co exist in the form of  $\text{Co}^{2+}$  and  $\text{Co}^{3+}$ . The binding energy at 798.3 and 783.1 eV represent  $\text{Co}^{2+}$ , and the peaks at 796.8 and 784.1 eV assign to  $\text{Co}^{3+}$ . The two broad peaks are located at 805.4 and 786.8 eV indexing satellite peaks. The O 1s spectrum of Fe-based colloidal electrodes (Figure 3c) and Ni/Co-based colloidal electrodes (Figure 3f) are deconvoluted into M–O. The XPS of F 1s and S 2p about positive and negative electrodes are shown in Figure S8. The presence of  $\text{F}^-$  can be attributed to the electrochemical reaction of  $\text{OH}^-$  in the electrolyte solution with  $\text{TFSI}^-$ , resulting in the degradation of  $\text{CF}_3$  groups in  $\text{TFSI}^-$  to form fluoride, which further prevents the electrolysis of water.<sup>[48]</sup>

$\text{FeCl}_3$  precursors were used to fabricate Fe negative electrodes. The potential window was measured by CV curves at a scan rate of 5  $\text{mV s}^{-1}$ . When the lowest potential decreases from  $-1.1$  to  $-1.4$  V versus SCE, obvious increase in current peak indicates the dominance of hydrogen evolution reaction (Figure 4a). Figure 4b shows the CV curves of  $\text{Fe}^{3+}$  negative electrode at scan rates from 5 to 50  $\text{mV/s}$ . All curves show quasi-rectangular shape between the potential window of  $-1.2$  and 0 V in 4 M KOH. No obvious change in shape is found at different scan rates. That means redox reaction having good reversibility. A linear relationship is obtained and shows in Figure 4c. The *b*-values of cathodic peak and anodic peak is 0.97. These values are between 0.5 and 1, indicating a mixed diffusion controlled and non-diffusion-limited capacitive process.

Similarly, the electrochemical performance of the cathode material was optimized. The electrochemical performance was tested using a three-electrode system in a 4 M electrolyte solution. For the cathode material precursor, the highest specific capacitance of 394.2 F/g at a current density of 1 A/g is obtained when the molar ratio of Ni to Co was 1:2 (Figure S9a). Compared with the specific capacitances of other electrode materials, Ni/Co-based colloidal electrode exhibits higher specific capacitances. At the same time, the volume of the precursor added was optimized. As shown in Figure S9c and S9d, the electrochemical performance of 10 and 15  $\mu\text{L}$  of precursor dissolved after cyclic voltammetric oxidation is not much different, so 10  $\mu\text{L}$  was selected. Ni/Co-based colloidal electrode were tested by cyclic voltammetry (CV) from 0 to 0.6 CV curves were performed at different scan rates (Figure 4d). A pair of redox peak is observed at various scan rates. For the analysis of the kinetic process of electrochemical reaction, a linear relationship ( $R^2 > 0.99$ ) was obtained according to a power law relationship ( $i_p = av^b$ ). Where  $i_p$  is the peak current, a

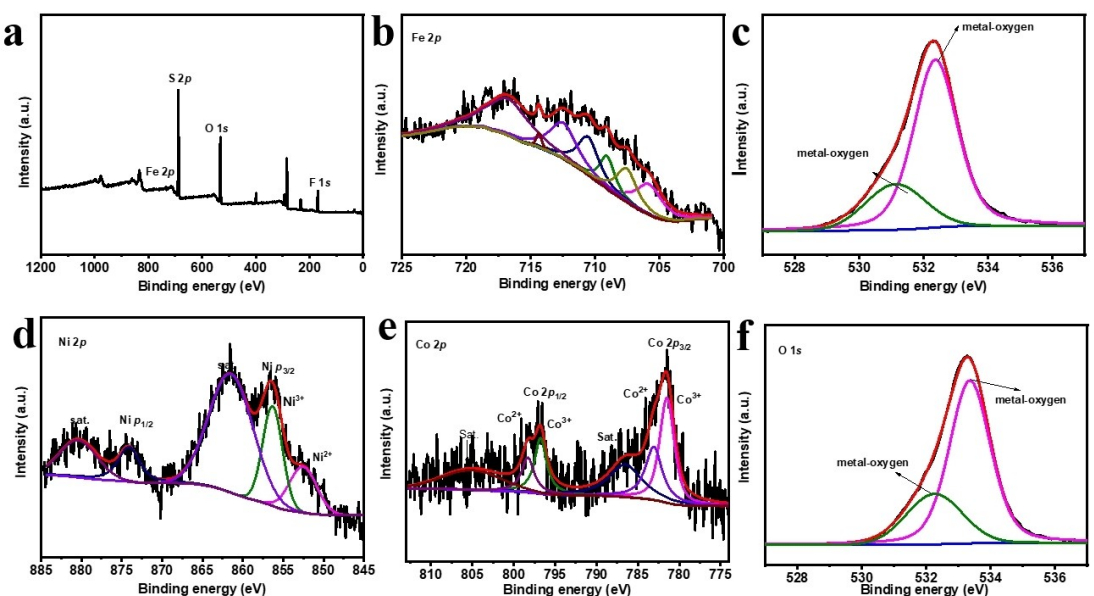
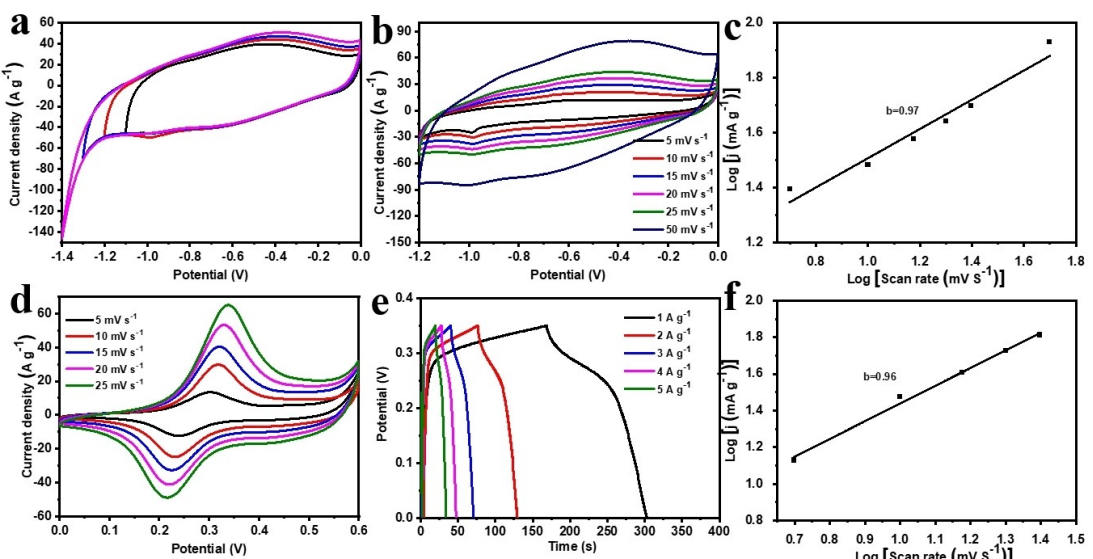


Figure 3. (a) XPS survey spectrum of Fe-based colloidal electrodes; Deconvoluted (b)  $\text{Fe } 2p$  and (c) O 1s. (d-f) XPS of Ni/Co-based colloidal electrodes; Deconvoluted (d)  $\text{Ni } 2p$ , (e)  $\text{Co } 2p$  and (f) O 1s.



**Figure 4.** (a) CV curves of Fe-based colloidal electrode obtained in different potential windows; (b) CV curves of Fe-based colloidal electrodes obtained at various scan rates from 5 to 50 mV/s; (c) Determination of the slope,  $b$  value, for the logarithm of anodic and cathodic peak current versus logarithm of scan rate from 5 to 50  $\text{mV s}^{-1}$ . (d) CV, (e) GCD curves, and (f) power law dependence of redox peak current on scan rate for Ni/Co-based colloidal electrode.

is a constant,  $v$  is the scan rate and the exponent  $b$  indicates the predominant kinetics mechanism. The  $b$ -values of cathodic peak is 0.96 (Figure 4f), indicating a mixed diffusion controlled and non-diffusion-limited capacitive process. The difference between anode peak potential and cathode peak potential increases with the increase of sweep speed, indicating that the reversibility of the reaction decreases. Moreover, the capacitive contribution was increased with an increased scan rate. But the non-diffusion -controlled mechanism was dominant at all scan rates. The GCD curves of Ni/Co-based colloidal electrode have shown in Figure 4e. The specific capacitances of Ni/Co-based colloidal electrode were 394.2, 312, 259.71, 228.4 and 208.5  $\text{F g}^{-1}$

at current density densities from 1 to 5  $\text{A g}^{-1}$ , respectively (Figure 4e).

The electrochemical performances of Ni/Co-based colloidal electrode // Fe-based colloidal electrode supercapattery in different concentrations of water in salt (LiTFSI-KOH) electrolyte are shown in Figure 5 and S10. Figure S10a shows that all CV curves with scan rates of 50 mV/s are similar, indicating the same energy storage mechanism. Figure S10b shows the GCD curves in different concentrations of electrolyte solutions, the results show that the working voltage can reach the highest 1.8 V when the concentration of LiTFSI is 0.05 mol/L KOH, which matches the CV curves. High concentrations of KOH

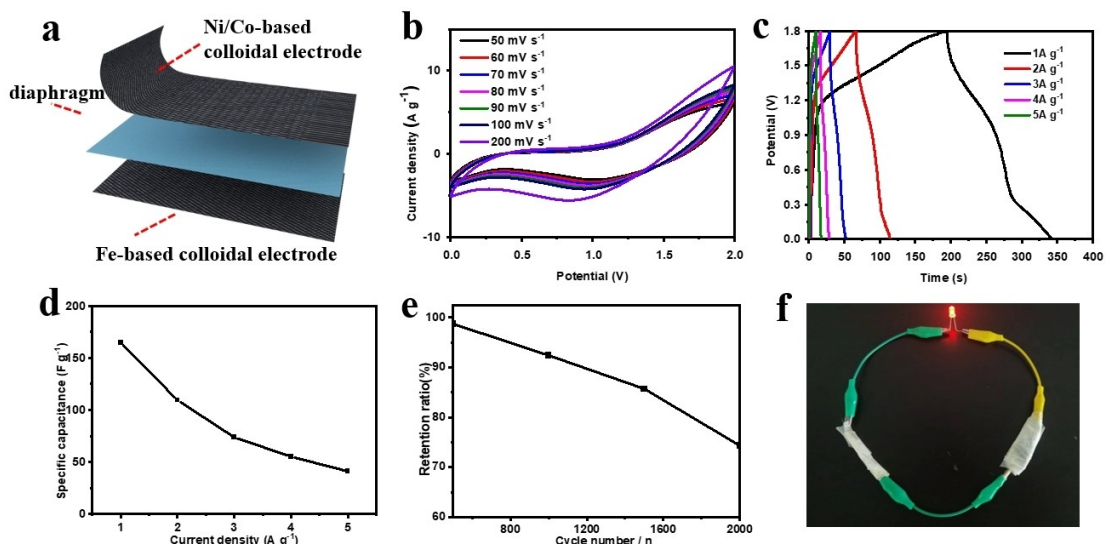


**Figure 5.** A series of electrochemical tests of Ni/Co-based colloidal electrode // Fe-based colloidal electrode supercapattery. The schematic diagram(a), CV (b), GCD (c) curve, (d) the corresponding specific capacitances at different current densities, cycle performance at the scan rate of  $2 \text{ A g}^{-1}$  of supercapattery (e). (f) Applying supercapattories to successfully light up a LED lamps.

exhibit poor electrochemical performance due to the fact that ion interactions are enhanced in high concentrations of electrolyte solutions, leading to a decrease in ion mobility and an increase in internal resistance, thereby reducing the efficiency of the capacitor's charging and discharging. For the assembled supercapattery, the LiTFSI-KOH electrolyte was sandwiched between the positive electrode of Ni/Co-based colloidal material and negative electrode of Fe-based colloidal material as shown in Figure 5a. The electrochemical performances of Ni/Co-based colloidal electrode // Fe-based colloidal electrode supercapattery were tested by CV, GCD and cycling stability measurements. The CV curves of the supercapattery with a potential window of 0–1.8 V at different scan rates from 50 to 200 mV/s are shown in Figure 5b. The GCD curves of Ni/Co-based colloidal electrode // Fe-based colloidal electrode supercapattery at current densities from 1 to 5 A/g are displayed in Figure 5c. According to the equation:  $C = I\Delta t / (m\Delta V)$ , the specific capacitance was 164.4, 109.3, 73.7, 55.11 and 41.1 A g<sup>-1</sup> at a current density of 1 to 5 A g<sup>-1</sup> (Figure 5d). And the energy density of Ni/Co-based colloidal electrode // Fe-based colloidal electrode supercapattery can reach up to 73.98 Wh kg<sup>-1</sup> at a power density of 1799.5 W kg<sup>-1</sup> based on the total mass of pristine salts. It is also higher than MnO<sub>2</sub>-TEA nanosheets (57.4 Wh kg<sup>-1</sup> at 450 W kg<sup>-1</sup>),<sup>[34]</sup> MnO<sub>2</sub>@Ni-HHTP (35.8 Wh kg<sup>-1</sup> at 600 W kg<sup>-1</sup>),<sup>[49]</sup> rGO/RuO<sub>2</sub> (31.1 Wh kg<sup>-1</sup> at 8365 W kg<sup>-1</sup>),<sup>[50]</sup> Fe-based CPs (40 Wh kg<sup>-1</sup> at 799 W kg<sup>-1</sup>)<sup>[51]</sup> in the current work with the other literatures. Finally, the cycling stability of the Ni/Co-based colloidal electrode // Fe-based colloidal electrode supercapattery was characterized by GCD measurement. As shown in Figure 5e, the specific capacitance of supercapattery still maintains 74.3% of the initial after 2000 cycles of GCD measurement. Two supercapatteries in series can light up a small LED light, indicating that supercapatteries have potential application value in energy storage (Figure 5f).

## Conclusions

In this work, a novel high-voltage aqueous supercapattery was developed by Ni/Co-based colloidal electrode as the positive electrode, Fe-based colloidal electrode as the negative electrode and LiTFSI-KOH as electrolyte. The maximum operating voltage of aqueous supercapattery is 1.8 V, and the energy density can reach 73.98 Wh kg<sup>-1</sup> at a power density of 1799.5 W kg<sup>-1</sup>. The electrolyte contains high concentrations of LiTFSI and KOH, releasing TFSI<sup>-</sup> surrounding water molecules, preventing water ionization and extending the stability of the system to 1.8 V. We have successfully demonstrated that LiTFSI can effectively broaden the electrochemical operating window in alkaline electrolytes. This increase in voltage is higher than the theoretical decomposition voltage of water. At the same time, thanks to the large specific surface area and the close connection with the conductive matrix, the new quasi-ionic electrode material has an unprecedented high specific capacity. Furthermore, this new combination of high-voltage electrolyte systems and novel ionic electrodes may be attractive for other energy storage systems. This wide-potential-window electrolyte

system can effectively improve the energy density of water energy storage devices.

## Experimental Section

### Materials

Nickel Chloride ((NiCl<sub>2</sub>·6H<sub>2</sub>O), Cobalt Chloride (CoCl<sub>2</sub>·6H<sub>2</sub>O), ferric chloride (FeCl<sub>3</sub>·6H<sub>2</sub>O), ammonium sulfate ((NH<sub>4</sub>)<sub>2</sub>SO<sub>4</sub>), bis(trifluoromethanesulfonyl)imide lithium salt (LiTFSI), ethanol and potassium hydroxide (KOH) were all of the analytical grades and used without any purification. The carbon cloth (CC) was purchased from CeTech Co. LTD.

### Preparation of Hydrophilic Carbon Cloth

The CC working as a collector was subjected to a 10 minutes ultrasound treatment in ethanol and ultrapure water. The cleaning carbon fabric was then immersed in 0.1 M (NH<sub>4</sub>)<sub>2</sub>SO<sub>4</sub> solution and electrochemically oxidized for 10 min under a constant potential of 15 V. During the electrochemical oxidation process, a large number of oxygen-containing functional groups were introduced on the surface of the carbon cloth to obtain HCC.

### Preparation of Electrode Materials and Electrolyte Solution

The preparation process of the electrolyte solution is as follows: different dosages of bis(trifluoromethanesulfonyl)imide lithium salt were gradually added into 2 mL 4 M KOH solution through vigorous stirring to form different concentrations of viscous solutions (0.1, 0.05, 0.066 and 0.4 mol). The preparation process of electrode materials is as follows: For cathode material, 0.237 g NiCl<sub>2</sub> and 0.237 g CoCl<sub>2</sub> were added to 10 mL H<sub>2</sub>O with stirring. For the anode material, 0.404 g FeCl<sub>3</sub>·6H<sub>2</sub>O were added to 10 mL H<sub>2</sub>O with stirring. After forming a uniform mixed solution, the appropriate amount of salt solutions was dried on HCC, and naturally dried at room temperature. Ni/Co-based colloidal material and Fe-based colloidal material were coated on the surface of HCC by the CV method in 120 cycles within a voltage window of 0~0.6 V and 0~1.2 V, respectively.

### Structural Characterization

The surface morphology and microstructure were observed by scanning electron microscope (SEM, Nova450). Elemental mapping analyses were used to analyze the existence of the elements. The crystal and chemical structures were investigated by laboratory X-ray diffraction (XRD, PANalytical XPert instrument) and X-ray photoelectron spectroscopy (XPS, K-Alpha +). The Fourier transform infrared (FTIR) spectra were characterized using PerkinElmer. Raman spectra were determined using the Reference 3000 + iRaman.

### Electrochemical Measurements and Characterization

The supercapacitor performances were tested using a CHI 660 E electrochemical workstation with a three-electrode and two-electrode system. The three-electrode setup was assembled by employing a saturated calomel reference electrode and platinum auxiliary electrode. Besides, 4 M KOH was selected as the electrolyte, while as-obtained products acted as the working electrode. In the three-electrode setup, Ni/Co-based colloidal electrode and Fe-based colloidal electrode acted as the working electrodes, the platinum wire and Hg/HgO served as the counter electrode and the

reference electrode, respectively, and LiTFSI-4 M KOH was served as the electrolyte. The specific capacitances of the electrode materials were obtained by the galvanostatic charge-discharge (GCD) curves, and the specific calculation formula is as follows:

$$C = \frac{i\Delta t}{m\Delta V} \quad (3)$$

where  $i$ ,  $\Delta t$ ,  $m$  and  $\Delta V$  represent current density (A), discharge time (s), the load mass of the active material (g) and the voltage range, respectively.

An asymmetrical device was assembled by using Ni/Co-based colloidal material and Fe-based colloidal material as positive and negative electrodes respectively and LiTFSI-4 M KOH was used as an electrolyte, and filter paper as the separator membrane. The specific capacitance ( $C_m$ , A g<sup>-1</sup>), the energy density (E, Wh/kg) and the power density (P, W/kg) were obtained according the following formula:

$$C_m = \frac{i\Delta t}{m\Delta V} \quad (4)$$

$$E = \frac{1}{2 \times 3.6} CV^2 \quad (5)$$

$$P = \frac{3600E}{t} \quad (6)$$

Where  $i$  is the current density (A g<sup>-1</sup>),  $t$  is discharge time (s),  $V$  is the operating voltage window (V).

## Acknowledgements

This work was supported by National Natural Science Foundation of China (52220105010). K.C. also acknowledges Qilu Young Scholars Program of Shandong University.

## Conflict of Interests

The authors declare no conflict of interest.

## Data Availability Statement

The data that support the findings of this study are available from the corresponding author upon reasonable request.

**Keywords:** Aqueous supercapacitor • Water-in-salt • High operating voltage • In situ electrochemical oxidation

- [1] Z. Wang, J. Chen, S. Sun, Z. Huang, X. Zhang, X. Li, H. Dong, *Energy Storage Mater.* **2022**, *50*, 161–185.
- [2] R. Y. Hu, L. Y. Liu, J. H. He, Y. Zhou, S. B. Wu, M. X. Zheng, M. Demir, P. P. Ma, *J. Energy Storage* **2023**, *72*, 108656.
- [3] S. Chai, W. Zhang, J. Yang, L. Zhang, X. Han, M. Theint, X. Ma, *J. Rare Earths* **2023**, *41*, 728–739.
- [4] F. Liu, M. Zhao, K. Chen, M. Hu, D. Xue, *CrystEngComm* **2023**, *25*, 2485–2492.
- [5] P. Simon, Y. Gogotsi, *Nat. Mater.* **2020**, *19*, 1151–1163.
- [6] G. F. Smaisim, A. M. Abed, H. Al-Madhhachi, S. K. Hadrawi, H. M. M. Al-Khateeb, E. Kianfar, *BioNanoScience* **2023**, *13*, 219–248.
- [7] M. Mansuer, L. Miao, Y. Qin, Z. Song, D. Zhu, H. Duan, Y. Lv, L. Li, M. Liu, L. Gan, *Chin. Chem. Lett.* **2023**, *34*, 107304.
- [8] H. Ren, L. Zhang, J. Zhang, T. Miao, R. Yuan, W. Chen, Z. Wang, J. Yang, B. Zhao, *Carbon* **2022**, *198*, 46–56.
- [9] G. Li, Y. Feng, Y. Yang, X. Wu, X. Song, L. Tan, *Nano Mater. Sci.* **2024**, *6*, 174–192.
- [10] J. Yan, Z. Fan, W. Sun, G. Ning, T. Wei, Q. Zhang, R. Zhang, L. Zhi, F. Wei, *Adv. Funct. Mater.* **2012**, *22*, 2632–2641.
- [11] F. Zhao, D. Zheng, Y. Liu, F. Pan, Q. Deng, C. Qin, Y. Li, Z. Wang, *Chem. Eng. J.* **2021**, *415*, 128871.
- [12] Q. Li, M. Liu, F. Huang, X. Zuo, X. Wei, S. Li, H. Zhang, *Chem. Eng. J.* **2022**, *437*, 135494.
- [13] S. Rahimpour, L. Luo, R. Teimuri-Mofrad, *Electrochimica Acta* **2022**, *416*, 140285.
- [14] H. Yu, X. Ge, C. Bulin, R. Xing, R. Li, G. Xin, B. Zhang, *Electrochimica Acta* **2017**, *253*, 239–247.
- [15] J. Yan, Q. Wang, T. Wei, Z. Fan, *Adv. Energy Mater.* **2014**, *4*, 1300816.
- [16] O. Karatum, E. Yildiz, H. N. Kaleli, A. Sahin, B. Ulgut, S. Nizamoglu, *Adv. Funct. Mater.* **2022**, *32*, 2109365.
- [17] A. G. Bagde, D. B. Malavekar, A. C. Lokhande, S. D. Khot, C. D. Lokhande, *J. Alloys Compounds* **2024**, *980*, 173591.
- [18] C.-H. Hsu, K.-H. Tseng, C.-Y. Hsu, D.-H. Chen, *Compos. B Eng.* **2023**, *252*, 110497.
- [19] S. Venkateswarlu, H. Mahajan, A. Panda, J. Lee, S. Govindaraju, K. Yun, M. Yoon, *Chem. Eng. J.* **2021**, *420*, 127584.
- [20] S. Ramanathan, M. SasiKumar, N. Radhika, A. Obadiah, A. Durairaj, G. Helen Swetha, P. Santhoshkumar, I. Sharmila Lydia, S. Vasanthkumar, *Mater. Today Proc.* **2021**, *47*, 843–852.
- [21] J. Lee, T. S. Lim, S. G. Jo, S. Jeong, H.-J. Paik, I. W. Ock, S. Lee, K. J. Yu, J. W. Lee, *Chem. Eng. J.* **2023**, *476*, 146515.
- [22] E. Payami, M. A. Keynezhad, K. D. Safa, R. Teimuri-Mofrad, *Electrochimica Acta* **2023**, *439*, 141663.
- [23] V. Raman, N. Clament Sagaya Selvam, S. B. Mitta, H.-K. Kim, *J. Alloys Compounds* **2024**, *971*, 172450.
- [24] M. Z. Ansari, I. Hussain, D. Mohapatra, S. A. Ansari, R. Rahighi, D. K. Nandi, W. Song, S.-H. Kim, *Adv. Sci.* **2024**, *11*, 2303055.
- [25] S. Wang, H. Xu, J. Zhao, Y. Li, *Inorg. Chem. Front.* **2022**, *9*, 514–523.
- [26] M. Zhu, Y. Huang, Y. Huang, Z. Pei, Q. Xue, H. Li, H. Geng, C. Zhi, *Adv. Funct. Mater.* **2016**, *26*, 4481–4490.
- [27] D. Mandal, P. Routh, A. K. Nandi, *Small* **2018**, *14*, 1702881.
- [28] Y. Lu, L. Li, D. Chen, G. Shen, *J. Mater. Chem. A* **2017**, *5*, 24981–24988.
- [29] J.-J. Zhou, Q. Li, C. Chen, Y.-L. Li, K. Tao, L. Han, *Chem. Eng. J.* **2018**, *350*, 551–558.
- [30] I. Rabani, R. Zafar, K. Subalakshmi, H.-S. Kim, C. Bathula, Y.-S. Seo, *J. Hazard. Mater.* **2021**, *407*, 124360.
- [31] D. Li, Y. Gong, M. Wang, C. Pan, *Nano-Micro Lett.* **2016**, *9*, 16.
- [32] S. Adhikari, S. Selvaraj, S.-H. Ji, D.-H. Kim, *Small* **2020**, *16*, 2005414.
- [33] Z. H. Huang, Y. Song, D. Y. Feng, Z. Sun, X. Sun, X. X. Liu, *ACS Nano* **2018**, *12*, 3557–3567.
- [34] A. Zhang, R. Zhao, L. Hu, R. Yang, S. Yao, S. Wang, Z. Yang, Y.-M. Yan, *Adv. Energy Mater.* **2021**, *11*, 2101412.
- [35] Z. Lv, Y. Luo, Y. Tang, J. Wei, Z. Zhu, X. Zhou, W. Li, Y. Zeng, W. Zhang, Y. Zhang, D. Qi, S. Pan, X. J. Loh, X. Chen, *Adv. Mater.* **2018**, *30*, 1704531.
- [36] S. Chen, H. Jiang, Q. Cheng, G. Wang, S. Petr, C. Li, *Chem. Eng. J.* **2021**, *403*, 126380.
- [37] P. Shi, L. Li, L. Hua, Q. Qian, P. Wang, J. Zhou, G. Sun, W. Huang, *ACS Nano* **2017**, *11*, 444–452.
- [38] J. Chen, J. Xu, S. Zhou, N. Zhao, C.-P. Wong, *Nano Energy* **2016**, *21*, 145–153.
- [39] S. V. Talande, A. Bakandritsos, P. Jakubec, O. Malina, R. Zbořil, J. Tuček, *Adv. Funct. Mater.* **2019**, *29*, 1906998.
- [40] X. Tian, Q. Zhu, B. Xu, *ChemSusChem* **2021**, *14*, 2501–2515.
- [41] F. Béguin, V. Presser, A. Balducci, E. Frackowiak, *Adv. Mater.* **2014**, *26*, 2219–2251.
- [42] S. Kumar, G. Saeed, L. Zhu, K. N. Hui, N. H. Kim, J. H. Lee, *Chem. Eng. J.* **2021**, *403*, 126352.
- [43] J.-Y. Luo, W.-J. Cui, P. He, Y.-Y. Xia, *Nat. Chem.* **2010**, *2*, 760–765.
- [44] X. Bu, L. Su, Q. Dou, S. Lei, X. Yan, *J. Mater. Chem. A* **2019**, *7*, 7541–7547.
- [45] H. Avireddy, B. W. Byles, D. Pinto, J. M. Delgado Galindo, J. J. Biendicho, X. Wang, C. Flox, O. Crosnier, T. Brousse, E. Pomerantseva, J. R. Morante, Y. Gogotsi, *Nano Energy* **2019**, *64*, 103961.
- [46] T. Nguyen, M. Fátima Montemor, *J. Mater. Chem. A* **2018**, *6*, 2612–2624.

- [47] J. Fang, C. Kang, L. Fu, S. Li, Q. Liu, *J. Alloys Compounds* **2020**, *849*, 156317.
- [48] N. Dubouis, P. Lemaire, B. Mirvaux, E. Salager, M. Deschamps, A. Grimaud, *Energy Environ. Sci.* **2018**, *11*, 3491–3499.
- [49] H. Duan, Z. Zhao, J. Lu, W. Hu, Y. Zhang, S. Li, M. Zhang, R. Zhu, H. Pang, *ACS Appl. Mater. Interfaces* **2021**, *13*, 33083–33090.
- [50] S. Korkmaz, İ. A. Kariper, O. Karaman, C. Karaman, *Ceram. Int.* **2021**, *47*, 34514–34520.
- [51] K. Wang, S. Wang, J. Liu, Y. Guo, F. Mao, H. Wu, Q. Zhang, *ACS Appl. Mater. Interfaces* **2021**, *13*, 15315–15323.

---

Manuscript received: June 12, 2024  
Revised manuscript received: July 19, 2024  
Accepted manuscript online: July 22, 2024  
Version of record online: September 23, 2024

---